Structural Basis of Synaptic Vesicle Assembly Promoted by α-Synuclein

Giuliana Fusco[1], Tillmann Pape[2], Amberley D. Stephens[3], Pierre Mahou[3,†], Ana Rita Costa[1], Clemens F. Kaminski[3], Gabriele S. Kaminski Schierle[3], Michele Vendruscolo[1], Gianluigi Veglia[4], Christopher M. Dobson[1,*] and Alfonso De Simone[2,*]

[1]Department of Chemistry, University of Cambridge, Cambridge CB2 1EW, UK

[2]Department of Life Sciences, Imperial College London, London SW7 2AZ, UK

[3]Department of Chemical Engineering and Biotechnology, University of Cambridge, Cambridge CB3 0HE, UK

[4]Department of Chemistry & Department of Biochemistry, Molecular Biology & Biophysics, University of Minnesota, Minneapolis, MN 55455, USA

[†]Current Address: Laboratory for Optics and Biosciences, Ecole Polytechnique, Palaiseau, 91128 Palaiseau Cedex, France.

To whom correspondence should be addressed: cmd44@cam.ac.uk or adesimon@imperial.ac.uk

Abstract

α-synuclein (αS) is an intrinsically disordered protein whose fibrillar aggregates are the major constituents of Lewy bodies in Parkinson's disease. Although the specific function of αS is still currently unclear, a general consensus is forming on its key role in regulating the process of neurotransmitter release, which is associated with the mediation of synaptic vesicle interactions and assembly. Here we report the analysis of wild type αS and two mutational variants linked to familial Parkinson's disease to describe the structural basis of a molecular mechanism enabling αS to induce the assembly of synaptic vesicles. We provide support for this 'double-anchor' mechanism by rationally designing and experimentally testing a further mutational variant of αS engineered to promote stronger interactions between synaptic vesicles. Our results characterise the nature of the active conformations of αS that mediate the clustering of synaptic vesicles, and indicate their relevance in both functional and pathological contexts.

Introduction

α-Synuclein (αS) is a 140-residue protein whose aggregation has been strongly associated with Parkinson's disease (PD)[1-5]. Fibrillar deposits of αS are the major constituents of Lewy bodies[6-8], a hallmark of the disease, and inherited forms of early onset PD are associated with mutations, duplications and triplications of the αS-encoding gene[9,10]. Despite the general consensus on its pathological relevance, the physiological role of αS remains widely debated. In this context, a view is emerging in which αS is involved in the dynamics of synaptic vesicles (SVs) trafficking by regulating a distal reserve pool of SVs that controls the amount of vesicles docked at the synapses during neurotransmitter release[11,12]. This biological role is directly associated with the ability of αS to bind to synaptic vesicles and induce their interaction and assembly *in vitro* and *in vivo*[13-16]. Indeed, in dopaminergic neurons αS exists in a tightly

45 regulated equilibrium[17] between a cytosolic monomeric form, which is predominantly
46 disordered[18-20], and a membrane-bound state, which is rich in α-helix structure in the region
47 spanning residue 1 to 90 of the protein sequence[15,21-26].

48 Because of its intrinsic ability to bind to a wide variety of biological membranes, the
49 physiological state of membrane-bound αS is extremely difficult to characterise, as a variety of
50 factors, including the presence of detergents[22] or chemical modifications of the protein[27], can
51 alter dramatically the structural properties of its bound state[15]. In a recent study, three major
52 regions were identified to have distinct structural and dynamical properties that influence in
53 different ways the nature of the membrane bound state of αS[28]; these regions include an N-
54 terminal α-helical segment, acting as the membrane-anchor, an unstructured C-terminal
55 region, weakly associated with the membrane, and a central region, undergoing order-
56 disorder transitions in the membrane-bound state and determining the affinity of αS for lipid
57 bilayers of different composition[28]. This structural variability indicates that it is of fundamental
58 importance to investigate the binding of αS to lipid membranes under conditions that
59 reproduce as closely as possible the physiological environment relevant to that of presynaptic
60 vesicles[15].

61 We describe here a detailed characterisation of the dynamical and structural properties at
62 the surface of synaptic-like lipid vesicles of two familial αS mutations that have opposite
63 effects on its affinity for membrane binding[29,30]. On the basis of these studies, we
64 characterised the details of the underlying mechanism by which a single molecule of αS binds
65 two different synaptic vesicles and promotes their interaction and assembly. This mechanism,
66 which involves a double-anchoring step enabling αS to form a dynamic link between two
67 vesicles, is strongly supported by an experiment in which a variant of αS was engineered to
68 adopt structural properties in its membrane bound state that result in enhanced αS-mediated
69 interactions between synaptic vesicles while maintaining the same amino-acid composition,
70 charge and membrane binding affinity of the wild type protein. The mechanism, which was
71 verified using both synthetic lipid vesicles and synaptic vesicles purified from rat brain,
72 provides evidence that the specific level of affinity for membrane binding of the non amyloid-β

73 component (NAC) region of αS is a fundamental functional property enabling this protein to
74 mediate the interaction between vesicles.

75

76 **Results**

77 **Binding of αS variants to membranes**

78 Using solution-state and solid-state nuclear magnetic resonance (NMR) spectroscopy in
79 combination with cryo-electron microscopy (cryo-EM) and stimulated emission depletion
80 (STED) imaging, we have characterised the structural properties at the surface of synaptic-like
81 vesicles of the familial αS mutants A30P[31] (αS_{A30P}) and E46K[32] (αS_{E46K}) and compared their
82 behaviour with that of the wild type protein (αS_{WT})[28]. In particular, we studied the interactions
83 of αS_{A30P}, αS_{E46K}, and αS_{WT} with small unilamellar vesicles (SUVs) composed of a mixture of
84 1,2-dioleoyl-sn-glycero-3-phosphoethanolamine (DOPE), 1,2-dioleoyl-sn-glycero-3-phospho-
85 L-serine (DOPS), and 1,2-dioleoyl-sn-glycero-3-phosphocholine (DOPC) in 5:3:2 molar
86 ratios[29], as such SUVs have been reported to be good mimics of synaptic vesicles for
87 composition and curvature[15]. The combination of magic angle spinning (MAS[33,34])
88 measurements in solid-state NMR (ssNMR[35]) and chemical exchange saturation transfer
89 (CEST[28,36-40], **Supplementary Fig. 1**) experiments in solution-state NMR used in this study
90 has already been shown to be highly effective in probing interactions between αS and SUVs,
91 enabling the degree of order and disorder in the membrane-bound state of αS_{WT} to be
92 characterised[28].

93 In the analysis of the interaction between αS_{A30P} and SUVs, CEST profiles (**Fig. 1** and
94 **Supplementary Fig. 2**) provided detailed information concerning the effects of the A30P
95 mutation, which was shown to reduce very substantially the binding affinity of αS for SUVs[15].
96 In αS_{A30P}, indeed, the binding of the N-terminal anchor region was found to involve a smaller
97 number of residues than in the case of αS_{WT} (residues 6-20 compared with residues 6-25 in
98 αS_{WT}) with generally a lower degree of CEST saturation than in the case of αS_{WT}. The major

99 differences between αS_{A30P} and αS_{WT} were evident in this membrane-anchor N-terminal
100 region, while the remainder of the protein sequence showed very limited variations in the
101 CEST profiles of these two proteins. The opposite behaviour was observed for the αS_{E46K}
102 variant, which binds SUVs with higher affinity than does αS_{WT}[15]. Indeed, the CEST data
103 indicate a significantly stronger interaction with the membrane for the N-terminal anchor
104 region of αS_{E46K}, which in this case extends up to residue 42 with a generally higher degree of
105 saturation than in the case of αS_{WT}. As with αS_{A30P}, minor variations in the CEST profiles were
106 also observed in other regions of the sequence of αS_{E46K}. The differences in the CEST
107 saturation profiles of the two mutants compared to αS_{WT} (**Supplementary Figs. 3 and 4**)
108 indicated more specifically that the major changes in the modes of binding to SUVs of these
109 mutational variants are associated primarily with the N-terminal region of the protein.

110 **Topology of αS_{A30P} and αS_{E46K} bound to SUVs**

111 In order to obtain detailed information on the topology of αS_{A30P} and αS_{E46K} when bound to
112 the surface of SUVs, we used MAS ssNMR experiments. ^{13}C-^{15}N labelled αS samples were
113 mixed with SUVs, as described previously,[15,28] to reach a protein:lipid ratio of 1:65[28]. Under
114 these conditions we could observe directly the resonances of both rigid and dynamical regions
115 of the membrane-bound αS molecule by using cross polarisation (CP) and insensitive nuclei
116 enhanced by polarization transfer (INEPT) experiments[41], respectively. In the CP regime, we
117 performed ^{13}C-^{13}C dipolar assisted rotational resonance (DARR)[42] measurements to detect
118 homonuclear correlations between carbon atoms of residues strongly anchored to the
119 membrane (**Fig. 2a**). In our previous study of αS_{WT}[28], the ^{13}C-^{13}C-DARR spectra identified
120 resonances of residues 6-25 of the anchor region, showing that this region folds into a highly
121 rigid α-helix lying essentially parallel to the membrane surface[28]. The ^{13}C-^{13}C-DARR spectra of
122 the membrane bound states of αS_{A30P} and αS_{E46K} are, however, substantially different from
123 those of αS_{WT}, indicating that the dynamical and structural properties of the anchor region vary
124 considerably between the wild type and variant forms of αS.

125 In the case of αS_{A30P}, the ^{13}C-^{13}C-DARR spectrum showed a very limited signal-to-noise
126 ratio and almost a complete absence of cross peaks, suggesting that the anchor region of this
127 variant is significantly more dynamic than the same region of the wild type protein. In contrast,
128 the ^{13}C-^{13}C DARR spectrum of αS_{E46K} showed a higher signal-to-noise ratio and a significantly
129 larger number of intense cross peaks, indicating an elongated anchor region in this mutational
130 variant that binds more strongly to SUVs. Using the dipolar connectivities from ^{15}N-^{13}C CP-
131 based experiments, along with our previous assignment of αS_{WT} and ^{13}C-^{13}C DARR spectra
132 acquired at different mixing times, we were able to assign individual spin systems in the ^{13}C-
133 ^{13}C DARR spectra of αS_{A30P} and αS_{E46K} (**Fig. 2a**). The chemical shifts were then compared to
134 those obtained from solution state NMR studies of αS_{WT} in SDS and SLAS micelles[22,43], and
135 indicated that, despite the differences in dynamics and in the binding strength relative to lipid
136 membranes, all the variants analysed here adopt a helical conformation at the N-terminal
137 anchor when bound to membranes. This finding is particularly relevant in the case of the A30P
138 mutation as it shows that, like the other variants and despite the insertion of a helix-breaker
139 residue, αS_{A30P} binds the lipid bilayer by adopting an amphipathic α-helix conformation at the
140 N-terminus and not as a disordered state that is tethered onto the lipid surface.

141 The highly dynamical regions of αS_{A30P} and αS_{E46K} bound to SUVs were then probed
142 directly by INEPT measurements acquired using MAS ssNMR experiments[41] and revealed ^{1}H-
143 ^{13}C correlations for resonances of the disordered C-terminal region of αS (**Fig. 2b**), which is
144 only weakly associated with the membrane[28]. In contrast to the results obtained from the
145 DARR spectra, no significant differences were found between αS_{A30P} and αS_{E46K} in the INEPT
146 spectra, indicating that the disordered C-terminal regions (residues 98-140) of the membrane-
147 bound states of these variants have similar structural and dynamical properties to those of
148 αS_{WT}. To gain further insights into the topological nature of mobile regions in the membrane-
149 bound αS_{A30P} and αS_{E46K} variants, we used paramagnetic relaxation enhancement (PREs)
150 experiments[28]. By doping the SUVs with low levels (2%) of a lipid carrying an unpaired
151 electron on the head group, namely the gadolinium salt of PE-DTPA (1,2-dimyristoyl-sn-
152 glycero-3-phosphoethanolamine-N-diethylenetriaminepentaacetic acid), we could observe

153 selective line broadening of individual resonances in the INEPT spectrum of both variants
154 (**Supplementary Fig. 5**), revealing those residues that interact transiently with the membrane
155 surface. The resulting broadening patterns of hydrophobic (including L100, A107, P108, I112,
156 L113, P117, V118, P120) and positively charged (K97 and K102) residues were found to be
157 similar to those observed in αS_{WT}. The selective broadening of the INEPT peaks of the C-
158 terminal residues in these PRE experiments is in agreement with mild levels of saturation
159 transfer that are detected for this region using CEST experiments performed with a bandwidth
160 of 350Hz and offset frequencies of ± 1.5 kHz (**Supplementary Fig. 4a**), which also provide
161 evidence for transient tethering of the C-terminal region of αS onto the membrane surface.

162 **Mechanism of vesicle assembly promoted by αS**

163 The solution-state and solid-state NMR measurements described above reveal a striking
164 degree of independence between the membrane binding properties of the N-terminal
165 membrane-anchor region of αS, which is significantly affected by the A30P and E46K
166 mutations, and of the region spanning residues 65 to 97, which instead shows negligible
167 differences as a result of these mutations (**Supplementary Figs. 3 and 4**). These
168 independent membrane-binding modes suggest that, in addition to interacting with the
169 membrane surface of the same SUV, these two regions are sufficiently independent to bind
170 simultaneously two different SUVs. Indeed our modelling studies show that a single αS
171 molecule could bind and bridge two vesicles that are as much as 150 Å apart (**Fig. 3a**), with
172 both the N-terminal anchor region (the N-terminal 25 residues) and the central region of αS
173 (residues 65 to 97) adopting the conformations of amphipathic α-helices. These data therefore
174 provide the structural basis of the mechanism by which αS promotes the interaction between
175 vesicles that has been observed experimentally both *in vitro*[14,15] and *in vivo*[13,16].

176 To obtain further evidence of this 'double-anchor' mechanism (**Fig. 3a**), we used our
177 findings to design a further variant of αS having structural properties that we anticipated
178 should enhance the probability of αS binding simultaneously to two different vesicles in such a
179 way as to mediate their interaction. In particular, to favour the double-anchor mechanism (**Fig.**

180 **3a**), this variant was designed to enhance the detachment of the region 65 to 97 from the
181 membrane surface when αS is bound to the SUVs *via* its N-terminal anchor region. We
182 identified for this purpose a swapped sequence (αS_{Sw}) incorporating the E46K and K80E
183 mutations (**Supplementary Fig. 6**). In particular, by replacing the lysine at position 80 with a
184 glutamic acid (K80E), the local binding to negatively charged vesicles is disfavoured, hence
185 shifting the conformational equilibrium of the fragment 65 to 97 towards a state where this
186 region is less strongly bound to the SUV surface. By contrast, because the K80E mutation
187 also affects the overall membrane affinity of αS, a second mutation in which the glutamic acid
188 at position 46 is replaced by a lysine (E46K) was selected to increase the interaction between
189 the N-terminal anchor region and the SUV surface, as probed in αS_{E46K} (**Figs. 1** and **2**),
190 thereby restoring an overall K_D comparable to that of the wild type protein.

191 We tested experimentally whether or not αS_{Sw} possessed the anticipated structural and
192 thermodynamical properties characteristic of its membrane-bound state. In agreement with
193 our design, we found the binding affinity of αS_{Sw} for SUVs, measured by circular dichroism
194 (CD)[28], to be similar to that of αS_{WT} (**Supplementary Fig. 7a-c**). By contrast the structural
195 properties of the αS_{Sw} variant, as probed by CEST (**Supplementary Fig. 7d-f**), showed a
196 significant reduction in the membrane interaction of the central region (residues 65 to 97) of
197 the variant than in αS_{WT}. These data indicate that αS_{Sw} binds SUVs with essentially the same
198 overall affinity as αS_{WT} but assumes different structural and dynamical properties in its bound
199 state that promote an enhanced exposure of the segment 65 to 97. CEST also confirmed the
200 stronger interaction of the anchor region of αS_{Sw} compared to that of αS_{WT}, which in the
201 designed variant is extended to residue 42 as a consequence of the E46K mutation
202 (**Supplementary Fig. 7e**). As αS_{Sw} and αS_{E46K} have the same sequence except at position 80,
203 we plotted the differences in the CEST profiles of these two variants; this comparison reveals
204 clearly that the binding properties of these two variants to the SUVs are indistinguishable
205 except in the region 65 to 97 (**Supplementary Fig. 8**) thereby providing additional evidence
206 for the independence of the membrane-binding properties of the N-terminal and central
207 regions in αS.

208 **Synaptic Vesicle assembly induced by αS_{WT} and αS_{Sw}**

209 We compared the efficiency with which αS_{Sw} and αS_{WT} promote the interaction and
210 assembly of vesicles by monitoring, using cryo-EM, the ability of the two variants to promote
211 coalescence and fusion of synaptic-like vesicles *in vitro*[16]. As a control, cryo-EM images of
212 0.05% DOPE:DOPS:DOPC SUVs incubated for 12 h in the absence of αS showed spherical
213 vesicles of diameters ranging between 30 nm and 60 nm, with negligible evidence of vesicle
214 fusion over the period of incubation (**Fig. 3b** and **Supplementary Fig. 9a**), showing that in the
215 absence of αS the spontaneous fusion of SUVs occurs with extremely slow kinetics. In the
216 presence of αS, however, the SUVs experience a considerable number of fusion events with
217 cryo-EM images revealing the presence of elongated fused vesicles having long axes of up to
218 200 nm under the conditions used in this study (**Fig. 3d** and **Supplementary Fig. 9b**).
219 Incubating SUVs with αS_{Sw}, however, resulted in a very significant increase in the extent of
220 vesicle fusion, with cryo-EM images clearly indicating that this variant is significantly more
221 active in promoting the interaction of SUVs ultimately leading to very large vesicle assemblies
222 (**Fig. 3f** and **Supplementary Fig. 9c**).

223 To generate a quantitative analysis of the sizes of the SUVs in the presence and absence
224 of the αS variants, we used STED microscopy imaging, which enabled us to sample rapidly
225 the sizes of thousands of vesicles to achieve statistically significant differences in the
226 distributions. STED imaging was carried out by fluorescently labelling the DOPE:DOPS:DOPC
227 SUVs with 2% of DOPE labelled with the ATTO 647N fluorophore. Images of isolated vesicles
228 resulted in a size distribution centred at 55 ± 11 nm (**Fig. 3c** and **Supplementary Figs. 10a-**
229 **b**), within the range anticipated from the preparation protocol[28]. However, STED images of
230 vesicles incubated with αS_{WT} clearly revealed the presence of numerous clusters of fused
231 lipids, whose sizes were quantified by using an algorithm that fits annular shapes to the lipid
232 vesicles, rather than the 2D Gaussian fitting used in the case of isolated vesicles (Methods
233 and **Supplementary Fig. 10**). The resulting distributions indicate that SUVs incubated with
234 αS_{WT} give rise to two populations of vesicles, one with properties similar to those of vesicles
235 imaged in the absence of αS and another attributable to fused vesicles, with a distribution

236 centred at 115 ± 30 nm and with a relative population of 16 % of the imaged vesicles (**Fig. 3e**
237 and **Supplementary Fig. 10c-d**).

238 Following incubation with αS_{Sw}, however, both the sizes and relative populations of the
239 fused vesicles increased dramatically, with the size distribution of fused vesicles now centred
240 at 181 ± 48 nm and with a relative population of 32 % of the imaged vesicles (**Fig. 3g** and
241 **Supplementary Figs. 10e-f**). Similar conclusions to those obtained from STED analysis were
242 obtained from measurements of dynamic light scattering (DLS), which showed that the
243 average size of the SUVs increases in the presence of αS and that this effect is considerably
244 greater with αS_{Sw} than with αS_{WT} (**Supplementary Fig. 11**). Overall, the cryo-EM, STED and
245 DLS data show that the engineered αS_{Sw} variant has a very significantly enhanced activity in
246 promoting the interactions between SUVs. As αS_{Sw} and αS_{WT} have the same amino acid
247 composition and net charge, and bind SUVs with similar thermodynamic affinity, the enhanced
248 interactions between vesicles upon incubation with αS_{Sw} can be attributed to the higher
249 population of conformations with an enhanced exposure of the region 65 to 97 from the
250 membrane surface, which increases the probability of associating with a different vesicle and
251 to mediate the vesicle assembly *via* a double-anchor mechanism (**Fig. 3a**), as probed by the
252 fusion of DOPE:DOPS:DOPC SUVs upon incubation with the protein (**Fig. 4**).

253 In order to assess the role of the double-anchor mechanism in the clustering of synaptic
254 vesicles (SVs) induced by αS, we incubated SVs purified from rat brain[44,45] for 48 h at 37 °C in
255 the presence or absence of αS samples (αS_{WT} or αS_{Sw}). The distribution of the sizes of the
256 clusters of SVs upon incubation were quantified using direct stochastic optical reconstruction
257 microscopy (*d*STORM)[46] to acquire images on poly-L-lysine-coated glass plates. In order to
258 visualise SVs, we used a primary antibody that is specific for the synaptic protein
259 synaptotagmin 1 and therefore binds selectively to SVs, and a secondary antibody
260 fluorescently labelled with ATTO 647N. The resulting *d*STORM images (**Fig. 5a-c**) were
261 analysed by identifying the centres of mass of each of the SVs and then by applying a
262 clustering approach[47] to identify groups of SVs that, according to a distance cutoff of 60 nm,
263 belong to the same cluster. The resulting distribution of sizes of SV clusters (**Fig. 5d**) showed

that 93% of the vesicles remain isolated after incubation for 48h at 37 °C in the absence of αS, with the remaining 6% and 1% assembled in clusters consisting of two and three SVs, respectively. After incubation under the same conditions but in the presence of 85 μM of αS_{WT}, up to 17% of the vesicles were clustered, some including assemblies composed up to 5 SVs (1%). In the presence of αS_{Sw}, however, over 29% of the vesicles were observed to be clustered up to 6 SVs (2%). Cryo-EM images of the assembled structures (**Fig. 5d**) revealed that the surfaces of the SVs composing the clusters are separated by distances that extend up to 15 nm, in agreement with the double-anchor mechanism (**Fig. 3a**).

Discussion

It is widely recognised that the physiological activity of αS is associated with its ability to bind to a variety of lipid membranes, including synaptic vesicles[48]. A number of studies support an emerging view that a key biological role of αS is to mediate the interactions and assembly of vesicles[14,16]. Vesicle clustering by αS has been shown to be a vital step in many functional processes, including ER-to-Golgi vesicle trafficking [13,49] and recycling of the SVs within the mechanism of neuronal communication[11]. In the present study we have examined the structural principles underlying the αS-induced interactions and assembly of SUVs by characterising the membrane binding properties of two mutational variants of αS linked with familial Parkinson's disease. This analysis reveals that two key regions of the protein, namely the N-terminal membrane-anchor (the N-terminal 25 residues) and the central region of the sequence (residues 65 to 97), have independent membrane binding properties and therefore are not only able to interact with a single SUV, but can also simultaneously bind to two different vesicles (**Fig. 3a**) thereby promoting their interaction and assembly as shown *in vitro* and *in vivo*[14-16]. The resulting double-anchor mechanism explains why the deletion of the segment 71-82 in the NAC region of αS or the impairment of the membrane affinity of the N-terminal anchor region of the protein severely affects *in vivo* vesicle clustering as shown in *S. cerevisiae*[16]. This mechanism also provides a structural explanation for the suggested loss of function caused by A30P, which is associated with an impairment of vesicle clustering by

292 αS_{A30P} as observed both *in vitro* and *in vivo*[14,16], as well as for the functional regulation
293 proposed to occur *via* the phosphorylation of serine 87 [50]. In particular, by introducing a
294 negative charge in the region 65 to 97, the phosphorylation of S87, which has been identified
295 both in functional contexts and in the case of synucleinopathies, has similar effects to those of
296 the K80E mutation in αS_{Sw}.

297 We tested this molecular mechanism by engineering a mutational variant of αS, called
298 αS_{Sw}, which was designed to enhance the probability of αS binding simultaneously to two
299 different vesicles. Our studies of this variant have provided strong evidence in support of the
300 proposed mechanism by showing that enhanced exposure of the central region, spanning
301 residues 65 to 97 in the membrane-bound state of αS, promotes more strongly the clustering
302 of SVs purified from rat brain (**Fig. 5**) and the assembly and fusion of DOPE:DOPS:DOPC
303 SUVs (**Fig. 4**). It has previously been suggested that a broken α-helix structural topology of
304 αS[22,51], which is a conformation that αS adopts upon binding to detergent micelles, could play
305 a role in vesicle-vesicle interactions stimulated by αS[48,52]. The present study, however, shows
306 experimentally that the underlying mechanism by which αS mediates the interactions between
307 lipid vesicles relies on the balance between ordered (membrane-bound) and disordered
308 (membrane-detached) conformational states of the region spanning residues 65 to 97 of the
309 protein. Perturbing this balance, as we have done rationally with αS_{Sw}, or upon alteration of
310 the expression levels of αS, can dramatically affect its ability to promote the vesicle assembly
311 *in vivo* leading to defects in the regulation of vesicle trafficking[11,13,49,53-57].

312 Other studies also suggest that αS could act as a molecular chaperone for the formation
313 of SNARE complexes, which appears to result from the direct interaction between αS and
314 synaptobrevin-2 at the surface of SVs[14,58]. Such an interaction was shown to be independent
315 of the NAC region, suggesting that this region has no direct functional role in this particular
316 process[59]. The present data, however, reveal that the NAC region is not only involved in αS
317 aggregation, as extensive evidence has previously indicated[4,60,61], but also has a specific role
318 in a key molecular mechanism associated with the normal function of αS. This study provides
319 evidence that the membrane affinity of the NAC region of αS is finely tuned to ensure an

320 optimal degree of local detachment from the membrane surface to enable binding to occur
321 between different vesicles. The present finding that, by perturbing this fine tuning through the
322 design of the αS_{Sw} variant, it is possible to promote stronger interactions between vesicles
323 (**Figs. 3 and 5**) indicates that the exposure of the region 65 to 97 in the vesicle-bound state of
324 αS is extremely crucial for the physiological mechanism of SVs clustering and, at least in the
325 case of αS_{Sw}, has more relevance than the local membrane binding affinity of the NAC region,
326 which in this variant is reduced as a result of the K80E mutation. The selection toward
327 sequence properties of αS that enable the detachment of the amyloidogenic NAC region from
328 the vesicle surface in order to favour the functional mechanism described in this study,
329 however, can also lead to aberrant behaviours, as these conformational states are particularly
330 vulnerable to self-association leading to αS aggregation at membrane surfaces[11,62-65]. Taken
331 together, these findings provide therefore a new mechanistic link between functional and
332 pathological roles of αS.
333

334 **Methods**

335 ***αS purification.*** αS_{WT} was expressed and purified in *Escerichia coli* using a pT7-7 plasmid in
336 which αS gene is under the control of the phage T7 RNA polymerase promoter. BL21 (DE3)-
337 gold competent cells (Agilent Technologies, Santa Clara, USA) were transformed with this
338 plasmid using heat-shock and subsequently grown in an isotope-enriched M9 minimal
339 medium containing 1 $g \cdot L^{-1}$ of ^{15}N ammonium chloride, 2 $g \cdot L^{-1}$ of ^{13}C-glucose and 100 $\mu g \cdot ml^{-1}$
340 ampicillin (Sigma-Aldrich, St Louis, USA) to produce uniformly ^{15}N and/or ^{13}C labelled αS
341 samples. Cell growth was carried at 37°C under constant shaking at 250 rpm to an OD600 of
342 0.6. Subsequently the expression of the protein was induced with 1mM isopropyl β-D-1-
343 thiogalactopyranoside (IPTG) at 37°C for 4h and cells were then harvested by centrifugation
344 at 6200*g* (Beckman Coulter, Brea, USA). The cell pellets were resuspended in lysis buffer
345 (10mM Tris-HCl pH 8, 1mM EDTA and EDTA-free complete protease inhibitor cocktail tablets
346 obtained from Roche, Basel, Switzerland) and lysed by sonication. The cell lysate was
347 centrifuged at 22,000*g* for 30 min to remove cell debris and the supernatant was then heated

348 for 20 min at 70°C and subsequently centrifuged at 22,000*g* in order to precipitate the heat-
349 sensitive proteins. Subsequently streptomycin sulfate was added to the supernatant to a final
350 concentration of 10 $mg \cdot ml^{-1}$ to stimulate DNA precipitation. The mixture was stirred for 15 min
351 at 4°C followed by centrifugation at 22,000*g*. Then, ammonium sulfate was added to the
352 supernatant to a concentration of 360 $mg \cdot ml^{-1}$ in order to precipitate the protein. The solution
353 was stirred for 30 min at 4°C and centrifuged again at 22,000*g*. The resulting pellet was
354 resuspended in 25 mM Tris-HCl, pH 7.7 and dialyzed against the same buffer in order to
355 remove salts. The dialyzed solutions were then loaded onto an anion exchange column (26/10
356 Q sepharose high performance, GE Healthcare, Little Chalfont, UK) and eluted with a 0 to 1 M
357 NaCl step gradient. αS was eluted at ~300 mM NaCl and then further purified by loading onto
358 a size exclusion column (Hiload 26/60 Superdex 75 preparation grade, GE Healthcare, Little
359 Chalfont, UK). All the fractions containing the monomeric protein were pooled together and
360 concentrated by using Vivaspin filter devices (Sartorius Stedim Biotech, Gottingen, Germany).
361 The purity of the aliquots after each step was analyzed by SDS-PAGE and the protein
362 concentration was determined from the absorbance at 275 nm using an extinction coefficient
363 of 5600 M^{-1} cm^{-1}.
364 In order to express and purify the mutational variants of αS (αS_{A30P}, αS_{E46K} and αS_{Sw}), we
365 employed the same experimental procedure as used in the case of αS_{WT}. Single point
366 mutations of the αS_{WT} plasmid were obtained using the Q5® Site-Directed Mutagenesis Kit
367 (New England Biolabs Inc., Ipswich, USA). Table 1 reports the primers employed to obtain the
368 plasmids of αS_{A30P}, αS_{E46K} and αS_{Sw}.
369
370 ***Preparation of synaptic-like SUVs.*** Small unilamellar vesicles (SUVs) containing a molar
371 ratio of 5:3:2 of DOPE:DOPS:DOPC (Avanti Polar Lipids Inc., Alabaster, USA) were prepared
372 from chloroform solutions of the lipids as described previously [15,28]. Briefly, the lipid mixture
373 was evaporated under a stream of nitrogen gas and then dried thoroughly under vacuum to
374 yield a thin lipid film. The dried thin film was re-hydrated by adding aqueous buffer (20 mM
375 sodium phosphate, pH 6.0) at a concentration of 15 $mg \cdot ml^{-1}$ (1.5%) and subjected to vortex
376 mixing. In all NMR experiments described in this paper SUVs were obtained by using several

cycles of freeze-thawing and sonication until the mixture became clear [15,28]. In the particular case of CEST experiments, SUVs at a concentration of 0.06% (0.6 $mg \cdot ml^{-1}$) were mixed with αS samples after sonication. For ssNMR studies αS was added to the SUV mixtures up to a molar ratio of 1:65 protein:lipid. The mixtures were then pelleted at 303,747*g* for 30 min at 4°C (Beckman Coulter Optima TLX Inc. Brea, USA) by using a TLA 100.3 rotor. Subsequently the SUV-αS samples were transferred into 3.2 mm Zirconia XC thin-walled MAS rotors for ssNMR experiments. For STED and Cryo-EM imaging experiments, as well as for DLS and kinetic measurements, DOPE:DOPS:DOPC SUVs were prepared by extrusion through membranes with a 50 nm pore diameter (Avanti Polar Lipids, Inc) after re-hydration in 20 mM sodium phosphate (pH 6.0) at a concentration of 1.0 $mg \cdot ml^{-1}$ (0.1%)

Purification of SVs from rat brain*.* SVs composed of phospholipid molecules (amounting to 30% of their composition), proteins (58%) and cholesterol (12%)[44,45] were purified from brains of rat provided by Charles River Laboratories (Animal work was approved by the Named Animal Care & Welfare Officer (NAWCO) and the Ethics Review Committee of the University of Cambridge). Rat brains were homogenised in 4mM HEPES and 320 mM sucrose buffer using protease inhibitors *via* ten strokes at 900 r.p.m. in glass-Teflon homogenizer (Wheaton, Millville, USA) [44,45]. All steps were carried out at 4°C or in ice. The homogenates were centrifuged at 1000*g* for 10 min and the supernatants were collected and further centrifuged at 15000*g* for 15 min. The supernatants from the second centrifugation (Sup-2) were stored at 4°C. The pellets from the second centrifugation, which contained the synaptosomes, were lysed using ice-cold water by applying three strokes at 2000 r.p.m. Subsequently, HEPES buffer solution containing protease inhibitors were added to the lysates and the resulting solutions were centrifuged at 17000 g for 15 min, and the supernatant was combined with the Sup-2 supernatants. The resulting mixtures were centrifuged at 48000*g* for 25 min and the supernatants were loaded onto a 0.7-M sucrose cushion and centrifuged at 133000*g* for 1 h. The bottom half of the sucrose cushion was pooled and centrifuged at 300000*g* for 2 h. The pellets were resuspended in buffer (100 mM Tris-HCl, pH 7.4, 100 mM KCl) and loaded onto a

405 Sephacryl S-1000 size-exclusion chromatography column (100 × 1 cm) resulting in a
406 distinctive peak of the SVs[44,45]. The SVs were then stained against specific SV antibodies,
407 including synaptotagmin 1, synaptobrevin 2, by western blot[44,45]. In order to perform *d*STORM
408 analyses, the SVs were incubated with a primary antibody (dilution 1:1000) that specifically
409 recognizes synaptotagmin 1 (105103, Synaptic Systems, Goettingen, DE) and a secondary
410 antibody (dilution 1:100) fluorescently labeled with Atto 647N (40839, Sigma-Aldrich, St Louis,
411 USA).
412
413 **Chemical exchange saturation transfer (CEST) experiments.** We employed CEST
414 measurements[28,36-38,40] to gain a deeper understanding of the equilibrium between membrane
415 unbound and membrane bound states of αS. In the study of αS-SUV interactions, CEST
416 shows enhanced characteristics compared to standard heteronuclear correlation
417 spectroscopy, including a significantly higher sensitivity at low lipid:protein ratios, conditions
418 under which protein or lipid aggregation can be minimised[64]. The resulting NMR signals
419 enable the interaction between αS and the membrane surface to be probed without
420 interference from additional factors that may influence the transverse relaxation rates of the
421 protein resonances[36-38,40]. In the CEST experiments employed here, a continuous weak
422 radiofrequency field (either 350 Hz or 170 Hz) was applied off-resonance (up to 28 kHz) in the
423 ^{15}N channel, thereby saturating the broad spectroscopic transitions in the bound
424 (undetectable) state but leaving the resonances of the free (detectable) state virtually
425 unperturbed[36-38,40]. The saturation of the bound state was then transferred to the free state *via*
426 chemical exchange, resulting in the attenuation of the intensities of the observable
427 resonances in the visible unbound state. By carrying out a series of experiments at various
428 offsets, it was possible to obtain a map of the strength of the interactions between the low (αS)
429 and high (SUVs) molecular weight species at a residue specific resolution.
430 Solution state NMR experiments were carried out at 10 °C on Bruker spectrometers
431 operating at ^{1}H frequencies of 700 MHz equipped with triple resonance HCN cryo-probes.
432 CEST experiments were based on ^{1}H-^{15}N HSQC experiments by applying constant wave
433 saturation in the ^{15}N channel. Since we aimed at probing the exchange between monomeric

αS (having sharp resonances) and αS bound to SUVs (having significantly broader resonances), a series of large offsets was employed (-28, -21, -14, -9, -5, -3, -1.5, 0, 1.5, 3, 5, 9, 14, 21 and 28 kHz), resulting in CEST profiles of symmetrical shapes (**Supplementary Fig. 1**) [28,36,37]. An additional spectrum, saturated at -100 kHz, was recorded as a reference. The CEST experiments were recorded using a data matrix consisting of 2048 (t_2, ^{1}H) × 220 (t_1, ^{15}N) complex points. Assignments of the resonances in ^{1}H-^{15}N-HSQC spectra of αS_{WT} were derived from our previous studies [28] whereas assignments of the mutational variants employed in this work were obtained by a standard combination of triple resonance solution NMR spectra [66].

Magic angle spinning (MAS) measurements*.* MAS provides complementary information to CEST as it allows the protein resonances in the vesicle-bound state, which is inaccessible to solution-state NMR, to be probed directly. MAS experiments were carried out on a 16.85T Bruker Spectrometer with a 3.2 mm E^{Free} probe. Dipolar assisted rotational resonance (DARR) experiments [42] were performed at a MAS rate of 10 kHz using a series of different mixing times (20, 50, 100, 200 and 500 ms), and the spectra were acquired at -19 ^{o}C and 4 ^{o}C (the latter for control experiments only) using a 1 ms contact time. Insensitive nuclei enhanced by polarization transfer (INEPT) spectra[41] were measured at 4 ^{o}C using a MAS rate of 10 kHz. Pulse widths were 2.5 μs for ^{1}H and 5.5 μs for ^{13}C, and ^{1}H TPPM decoupling was applied at $\omega RF/(2\pi)$ = 71.4-100 kHz [28].

Cryo-electron microscopy (cryo-EM) measurements*.* All samples used in cryo-EM measurements were incubated, with or without αS (200 μM), for 12h at 298K using fresh preparations of DOPE:DOPS:DOPC SUVs at a concentration of 0.05%. After incubation cryo-EM grids were prepared by vitrifying the sample solutions using aliquots of 2 μL and a Vitrobot Mark III apparatus (SMIF, Duke University, Durham, USA) at a relative humidity of 100%. The samples were loaded on a glow-discharged Quantifoil R2/2 (Quantifoil GmbH, Germany) and blotted with filter paper for 2.5 s to leave a thin film of solution. The blotted samples were immediately plunged into liquid ethane and stored under liquid nitrogen prior to imaging.

463 Samples were examined using a Philips CM200 FEG electron microscope operating at 200 kV
464 (Philips, Amsterdam, the Netherlands), using a Gatan 626 cryo-holder (Gatan, Pleasantos,
465 USA) cooled with liquid nitrogen to temperatures below −180 °C. Digital images were acquired
466 on a TVIPS FC415 CCD camera using the EMMENU 4 software package (TVIPS, Munich,
467 Germany).
468
469 **Stimulated emission depletion (STED) microscopy.** STED imaging [67,68] was carried out by
470 fluorescently labelling the DOPE:DOPS:DOPC SUVs with 2% of fluorescently labelled DOPE
471 (ATTO 647N DOPE, ATTO-TECH, USA). STED microscopy allows the diffraction limit in
472 optical microscopy (~200nm) to be overcome [69] and imaging was performed on a home-built
473 pulsed STED microscope [69] using a single titanium-sapphire oscillator centered at λ_{STED} =
474 765 nm (Ti:S, Mai Tai HP, Spectra-physics, Santa Clara, USA) to generate the STED beam,
475 which was subsequently split into two using a half-plate and a polarisation beam splitter. Of
476 these two beams, the one transmitted was focused onto a photonic crystal fiber (FemtoWhite,
477 NKT Photonics, Cologne, Germany) to produce white light radiation. From this light, an
478 excitation beam, centered at λ_{Exc} = 640 nm, was extracted using a bandpass filter (637/7
479 BrightLine HC, Semrock, New York, USA) and coupled into a 30 m long polarization
480 maintaining single-mode fiber (PM630-HP, Thorlabs, Newton, UK). The reflected STED beam
481 was passed through a 50 cm long glass block of SF66 and a 100 m long polarization
482 maintaining single-mode fiber (PM-S630-HP, Thorlabs, Newton, UK) to stretch the pulse
483 duration to approximately 100-200 ps. Additionally the STED beam was converted into a so
484 called donut beam by a spatial light modulator (X10468−02, Hamamatsu Photonics,
485 Hamamatsu City, Japan). The excitation and STED beams were recombined with a dichroic
486 mirror (T735spxr, Chroma, Bellow Falls, USA) and detected using a commercial
487 point-scanning microscope (Abberior Instruments, Gottingen, Germany) comprising of a
488 microscope frame (IX83, Olympus, Shinjiuku, Japan), a set of galvanometer mirrors (Quad
489 scanner, Abberior Instruments, Gottingen, Germany) and a detection unit. The beams were
490 focused onto the sample by a 100x/1.4 NA oil immersion objective lens (UPLSAPO 100XO,
491 Olympus, Gottingen, Germany) and images were acquired by raster scanning the beams

492 across the sample using the Inspector software (Andreas Schönle, Max Planck Institute for
493 Biophysical Chemistry, Göttingen, Germany). We used a field of view of $30 \times 30\ \mu m^2$ with a
494 pixel size of $15 \times 15\ nm^2$ and a pixel dwell time of 20 μs. Fluorescence photons emerging from
495 the sample were collected by the microscope objective lens, de-scanned by the galvanometer
496 mirrors, focused onto a pinhole and detected using an avalanche photodiode (SPCM-AQRH,
497 Excelitas Technologies. Waltham, USA). The laser powers, measured at the objective back
498 aperture, were ca. 20 μW and 150 mW for the excitation beam and for the STED beam,
499 respectively.

500

501 **Analysis of STED images for vesicle size measurement.** Vesicle sizes were estimated
502 from STED images by using in-house Matlab scripts (**Supplementary data 1**). First, images
503 of isolated vesicles were identified and analysed using a fitting based on a 2D Gaussian
504 function, by convolving the images with a Gaussian filter whose dimensions match the
505 extension of the expected STED point spread function. The centres of the vesicles were
506 identified by finding local maxima of the convolved images, excluding the local maxima
507 corresponding to fused vesicles by means of a threshold applied on the peak intensities. A
508 different fitting procedure was optimised in the case of assembled vesicles that appear as
509 hollow shapes in the STED images, as for a vesicle larger than the lateral resolution of the
510 STED microscope the number of dye molecules probed increase on the edge of the shell. To
511 estimate the size of the clusters and their relative number compared to the non-fused vesicles,
512 all the vesicles appearing as fused were fitted by annular functions having a Gaussian radial
513 profile (amplitude, position, radius and offset) using a nonlinear least squares approach.

514

515 **Direct stochastic optical reconstruction microscopy (dSTORM).** Super-resolution imaging
516 was performed using *d*STORM microscopy with a Nikon Eclipse TE 300 inverted wide-field
517 microscope using a 100 X, 1.49-N.A total internal reflection fluorescence (TIRF)[46] objective
518 lens (Nikon, UK Ltd.). The vesicle and αS samples were adhered to a glass coverslip coated
519 in poly-L-lysine (P4707, Sigma Aldrich) before photoswitching buffer solution was added,
520 consisting of 100 mM mercaptoethylamine (MEA) in phosphate buffered saline (PBS, pH 8.2).

521 For imaging, a laser emitting at a wavelength of 640 nm was used (Toptica Photonics AG,
522 Graefelfing, Germany) for excitation of the Atto 647N dye. A 405 nm laser (Mitsubishi S3
523 Electronics Corp., Tokyo, Japan) was used as the reactivation source, which was only turned
524 on when the number of active fluorophores in the field of view was visibly reduced. Imaging
525 was performed under TIRF illumination conditions, ensuring that the exact centre of the field
526 of view, FOV, was illuminated. The FOV covered 1997 × 1997 camera pixels, corresponding to
527 an area on the sample of ~20 × 20 μm^2. 10,000 fluorescence frames were recorded, each
528 corresponding to an exposure time of 10 ms; the latter was matched to be in the range of the
529 average "on" time of the fluorescent dyes. The fluorescence light in the detection path was
530 filtered and imaged with an Ixon DV887 ECS-BV EM-CCD camera (Andor, UK).The image
531 analysis was performed using frames 1,000 to 10,000 in each sequence. From each image
532 stack, a reconstructed *d*STORM image was generated using the open-source rapidSTORM
533 software (**Supplementary Data 2**) developed in house using MATLAB (The MathWorks, Inc.).
534
535 **Dynamic light scatterning (DLS).** DLS measurements of vesicle size distributions were
536 performed using a Zetasizer Nano ZSP instrument (Malvern Instruments, Malvern, UK) with
537 backscatter detection at a scattering angle of 173°. The viscosity (0.8882 cP) and the
538 refractive index (1.330) of water were used as parameters for the buffer solution, and the
539 material properties of the analyte were set to those of the lipids (absorption coefficient of
540 0.001 and refractive index of 1.440). SUVs were used at a concentration of 0.05% in these
541 measurements and the experiments were performed at 25 °C. The acquisition time for the
542 collection of each dataset was 10 sec and accumulation of the correlation curves was
543 obtained using 10 repetitions. Each measurement was repeated 10 times to estimate standard
544 deviations and average values of the centres of the size distributions (**Supplementary Fig.
545 11**).
546
547 **Modelling.** Schematic representations of αS bound to SUVs were obtained by using
548 molecular dynamics (MD) simulations in implicit solvent. The structure of αS in the double-
549 anchoring mechanism (**Fig. 3a**) were obtained by starting from the model of membrane-bound

550 conformation αS characterised by an elongated helix (residues 1 to 97) with a disordered C-
551 terminal region (residues 98 to 140) which was part of the ensemble characterised
552 previously[28]. Atomic coordinates (in Cartesian space) of the N-terminal anchor were
553 harmonically restrained to maintain a fixed position whereas the region spanning residues 65
554 to 97 was restrained in the alpha-helical. A constant force along the membrane normal was
555 applied to this region to extend it toward the second vesicle (up in the **Fig. 3a**). The reminder
556 of the protein (residues 26 to 59 and 98 to 140) was allowed to relax under the Newtonian
557 laws of motions during the MD simulations. Curved vesicle surfaces were generated by
558 starting from atomic models of DOPE:DOPS:DOPC bilayers and by generating roto-
559 translations that imposed a spherical symmetry with a radius of 25 nm.

560

561 **Data Availability.** Data supporting the findings of this study are available within the article and
562 its supplementary information files and from the corresponding author upon reasonable
563 request.

564 **References**

565 1 Luk, K. C. *et al.* Pathological alpha-synuclein transmission initiates Parkinson-like
566 neurodegeneration in nontransgenic mice. *Science* **338**, 949-953, (2012).

567 2 Dobson, C. M. Protein folding and misfolding. *Nature* **426**, 884-890, (2003).

568 3 Uversky, V. N. & Eliezer, D. Biophysics of Parkinson's disease: structure and
569 aggregation of alpha-synuclein. *Curr Protein Pept Sci* **10**, 483-499, (2009).

570 4 Chiti, F. & Dobson, C. M. Protein misfolding, functional amyloid, and human disease.
571 *Annu Rev Biochem* **75**, 333-366, (2006).

572 5 Luth, E. S., Stavrovskaya, I. G., Bartels, T., Kristal, B. S. & Selkoe, D. J. Soluble,
573 prefibrillar alpha-synuclein oligomers promote complex I-dependent, Ca2+-induced
574 mitochondrial dysfunction. *J Biol Chem* **289**, 21490-21507, (2014).

575 6 Goedert, M., Spillantini, M. G., Del Tredici, K. & Braak, H. 100 years of Lewy
576 pathology. *Nat Rev Neurol* **9**, 13-24, (2013).

577 7 Bosco, D. A. *et al.* Elevated levels of oxidized cholesterol metabolites in Lewy body
578 disease brains accelerate alpha-synuclein fibrilization. *Nat Chem Biol* **2**, 249-253,
579 (2006).

580 8 Jucker, M. & Walker, L. C. Self-propagation of pathogenic protein aggregates in
581 neurodegenerative diseases. *Nature* **501**, 45-51, (2013).

582 9 Polymeropoulos, M. H. *et al.* Mutation in the alpha-synuclein gene identified in families
583 with Parkinson's disease. *Science* **276**, 2045-2047, (1997).

584 10 Singleton, A. B. *et al.* alpha-Synuclein locus triplication causes Parkinson's disease.
585 *Science* **302**, 841, (2003).

586 11 Auluck, P. K., Caraveo, G. & Lindquist, S. alpha-Synuclein: membrane interactions
587 and toxicity in Parkinson's disease. *Annu Rev Cell Dev Biol* **26**, 211-233, (2010).

588 12 Wislet-Gendebien, S. *et al.* Cytosolic proteins regulate alpha-synuclein dissociation
589 from presynaptic membranes. *J Biol Chem* **281**, 32148-32155, (2006).

590 13 Gitler, A. D. *et al.* The Parkinson's disease protein alpha-synuclein disrupts cellular
591 Rab homeostasis. *Proc Natl Acad Sci U S A* **105**, 145-150, (2008).

592 14 Diao, J. *et al.* Native alpha-synuclein induces clustering of synaptic-vesicle mimics via
593 binding to phospholipids and synaptobrevin-2/VAMP2. *Elife* **2**, e00592, (2013).

594 15 Bodner, C. R., Dobson, C. M. & Bax, A. Multiple tight phospholipid-binding modes of
595 alpha-synuclein revealed by solution NMR spectroscopy. *J Mol Biol* **390**, 775-790,
596 (2009).

597 16 Soper, J. H. *et al.* Alpha-synuclein-induced aggregation of cytoplasmic vesicles in
598 Saccharomyces cerevisiae. *Mol Biol Cell* **19**, 1093-1103, (2008).

599 17 Lee, H. J., Choi, C. & Lee, S. J. Membrane-bound alpha-synuclein has a high
600 aggregation propensity and the ability to seed the aggregation of the cytosolic form. *J*
601 *Biol Chem* **277**, 671-678, (2002).

602 18 Weinreb, P. H., Zhen, W., Poon, A. W., Conway, K. A. & Lansbury, P. T., Jr. NACP, a
603 protein implicated in Alzheimer's disease and learning, is natively unfolded.
604 *Biochemistry* **35**, 13709-13715, (1996).

605 19 Theillet, F. X. *et al.* Structural disorder of monomeric alpha-synuclein persists in
606 mammalian cells. *Nature* **530**, 45-50, (2016).

607 20 Felli, I. C., Gonnelli, L. & Pierattelli, R. In-cell (1)(3)C NMR spectroscopy for the study
608 of intrinsically disordered proteins. *Nat Protoc* **9**, 2005-2016, (2014).

609 21 Maltsev, A. S., Ying, J. & Bax, A. Impact of N-terminal acetylation of alpha-synuclein
610 on its random coil and lipid binding properties. *Biochemistry* **51**, 5004-5013, (2012).

611 22 Ulmer, T. S. & Bax, A. Comparison of structure and dynamics of micelle-bound human
612 alpha-synuclein and Parkinson disease variants. *J Biol Chem* **280**, 43179-43187,
613 (2005).

614 23 Kang, L. *et al.* N-terminal acetylation of alpha-synuclein induces increased transient
615 helical propensity and decreased aggregation rates in the intrinsically disordered
616 monomer. *Protein Sci* **21**, 911-917, (2012).

617 24 Maltsev, A. S., Chen, J., Levine, R. L. & Bax, A. Site-specific interaction between
618 alpha-synuclein and membranes probed by NMR-observed methionine oxidation rates.
619 *J Am Chem Soc* **135**, 2943-2946, (2013).

620 25 Leftin, A., Job, C., Beyer, K. & Brown, M. F. Solid-state (1)(3)C NMR reveals annealing
621 of raft-like membranes containing cholesterol by the intrinsically disordered protein
622 alpha-Synuclein. *J Mol Biol* **425**, 2973-2987, (2013).

623 26 Fauvet, B. *et al.* Characterization of semisynthetic and naturally Nalpha-acetylated
624 alpha-synuclein in vitro and in intact cells: implications for aggregation and cellular
625 properties of alpha-synuclein. *J Biol Chem* **287**, 28243-28262, (2012).

626 27 Jao, C. C., Hegde, B. G., Chen, J., Haworth, I. S. & Langen, R. Structure of
627 membrane-bound alpha-synuclein from site-directed spin labeling and computational
628 refinement. *Proc Natl Acad Sci U S A* **105**, 19666-19671, (2008).

629 28 Fusco, G. *et al.* Direct observation of the three regions in alpha-synuclein that
630 determine its membrane-bound behaviour. *Nat Commun* **5**, 3827, (2014).

631 29 Bodner, C. R., Maltsev, A. S., Dobson, C. M. & Bax, A. Differential phospholipid
632 binding of alpha-synuclein variants implicated in Parkinson's disease revealed by
633 solution NMR spectroscopy. *Biochemistry* **49**, 862-871, (2010).

634 30 Bussell, R., Jr. & Eliezer, D. Effects of Parkinson's disease-linked mutations on the
635 structure of lipid-associated alpha-synuclein. *Biochemistry* **43**, 4810-4818, (2004).

636 31 Kruger, R. *et al.* Ala30Pro mutation in the gene encoding alpha-synuclein in
637 Parkinson's disease. *Nat Genet* **18**, 106-108, (1998).

638 32 Zarranz, J. J. *et al.* The new mutation, E46K, of alpha-synuclein causes Parkinson and
639 Lewy body dementia. *Ann Neurol* **55**, 164-173, (2004).

640 33 Su, Y., Andreas, L. & Griffin, R. G. Magic angle spinning NMR of proteins: high-
641 frequency dynamic nuclear polarization and (1)H detection. *Annu Rev Biochem* **84**,
642 465-497, (2015).

643 34 Reif, B. Ultra-high resolution in MAS solid-state NMR of perdeuterated proteins:
644 implications for structure and dynamics. *J Magn Reson* **216**, 1-12, (2012).

645 35 Baker, L. A. & Baldus, M. Characterization of membrane protein function by solid-state
646 NMR spectroscopy. *Curr Opin Struct Biol* **27**, 48-55, (2014).

647 36 Huang, H., Milojevic, J. & Melacini, G. Analysis and optimization of saturation transfer
648 difference NMR experiments designed to map early self-association events in
649 amyloidogenic peptides. *J Phys Chem B* **112**, 5795-5802, (2008).

650 37 Fawzi, N. L., Ying, J., Ghirlando, R., Torchia, D. A. & Clore, G. M. Atomic-resolution
651 dynamics on the surface of amyloid-beta protofibrils probed by solution NMR. *Nature*
652 **480**, 268-272, (2011).

653 38 Vallurupalli, P., Bouvignies, G. & Kay, L. E. Studying "invisible" excited protein states
654 in slow exchange with a major state conformation. *J Am Chem Soc* **134**, 8148-8161,
655 (2012).

656 39 Sekhar, A., Rosenzweig, R., Bouvignies, G. & Kay, L. E. Mapping the conformation of
657 a client protein through the Hsp70 functional cycle. *Proc Natl Acad Sci U S A* **112**,
658 10395-10400, (2015).

659 40 Milojevic, J., Esposito, V., Das, R. & Melacini, G. Understanding the molecular basis
660 for the inhibition of the Alzheimer's Abeta-peptide oligomerization by human serum
661 albumin using saturation transfer difference and off-resonance relaxation NMR
662 spectroscopy. *J Am Chem Soc* **129**, 4282-4290, (2007).

663 41 Morris, G. A. & Freeman, R. Enhancement of Nuclear Magnetic-Resonance Signals by
664 Polarization Transfer. *Journal of the American Chemical Society* **101**, 760-762, (1979).

665 42 Takegoshi, K. & Terao, T. 13C-1H dipolar recoupling under very fast magic-angle
666 spinning using virtual pulses. *Solid State Nucl Magn Reson* **13**, 203-212, (1999).

667 43 Rao, J. N., Jao, C. C., Hegde, B. G., Langen, R. & Ulmer, T. S. A combinatorial NMR
668 and EPR approach for evaluating the structural ensemble of partially folded proteins. *J*
669 *Am Chem Soc* **132**, 8657-8668, (2010).

670 44 Ahmed, S., Holt, M., Riedel, D. & Jahn, R. Small-scale isolation of synaptic vesicles
671 from mammalian brain. *Nat Protoc* **8**, 998-1009, (2013).

672 45 Takamori, S. *et al.* Molecular anatomy of a trafficking organelle. *Cell* **127**, 831-846,
673 (2006).

674 46 Pinotsi, D. *et al.* Nanoscopic insights into seeding mechanisms and toxicity of alpha-
675 synuclein species in neurons. *Proc Natl Acad Sci U S A*, (2016).

676 47 De Simone, A. *et al.* Intrinsic disorder modulates protein self-assembly and
677 aggregation. *Proc Natl Acad Sci U S A* **109**, 6951-6956, (2012).

678 48 Snead, D. & Eliezer, D. Alpha-synuclein function and dysfunction on cellular
679 membranes. *Exp Neurobiol* **23**, 292-313, (2014).

680 49 Cooper, A. A. *et al.* Alpha-synuclein blocks ER-Golgi traffic and Rab1 rescues neuron
681 loss in Parkinson's models. *Science* **313**, 324-328, (2006).

682 50 Paleologou, K. E. *et al.* Phosphorylation at S87 is enhanced in synucleinopathies,
683 inhibits alpha-synuclein oligomerization, and influences synuclein-membrane
684 interactions. *J Neurosci* **30**, 3184-3198, (2010).

685 51 Mazumder, P., Suk, J. E. & Ulmer, T. S. Insight into alpha-synuclein plasticity and
686 misfolding from differential micelle binding. *J Phys Chem B* **117**, 11448-11459, (2013).

687 52 Dikiy, I. & Eliezer, D. Folding and misfolding of alpha-synuclein on membranes.
688 *Biochim Biophys Acta* **1818**, 1013-1018, (2012).

689 53 Nemani, V. M. *et al.* Increased expression of alpha-synuclein reduces neurotransmitter
690 release by inhibiting synaptic vesicle reclustering after endocytosis. *Neuron* **65**, 66-79,
691 (2010).

692 54 Abeliovich, A. *et al.* Mice lacking alpha-synuclein display functional deficits in the
693 nigrostriatal dopamine system. *Neuron* **25**, 239-252, (2000).

694 55 Outeiro, T. F. & Lindquist, S. Yeast cells provide insight into alpha-synuclein biology
695 and pathobiology. *Science* **302**, 1772-1775, (2003).

696 56 Tardiff, D. F., Khurana, V., Chung, C. Y. & Lindquist, S. From yeast to patient neurons
697 and back again: powerful new discovery platform. *Mov Disord* **29**, 1231-1240, (2014).

698 57 Cabin, D. E. *et al.* Synaptic vesicle depletion correlates with attenuated synaptic
699 responses to prolonged repetitive stimulation in mice lacking alpha-synuclein. *J*
700 *Neurosci* **22**, 8797-8807, (2002).

701 58 Burre, J. *et al.* Alpha-synuclein promotes SNARE-complex assembly in vivo and in
702 vitro. *Science* **329**, 1663-1667, (2010).

703 59 Burre, J., Sharma, M. & Sudhof, T. C. Systematic mutagenesis of alpha-synuclein
704 reveals distinct sequence requirements for physiological and pathological activities. *J*
705 *Neurosci* **32**, 15227-15242, (2012).

706 60 Cookson, M. R. The biochemistry of Parkinson's disease. *Annu Rev Biochem* **74**, 29-
707 52, (2005).

708 61 Rodriguez, J. A. *et al.* Structure of the toxic core of alpha-synuclein from invisible
709 crystals. *Nature* **525**, 486-490, (2015).

710 62 Grey, M., Linse, S., Nilsson, H., Brundin, P. & Sparr, E. Membrane interaction of
711 alpha-synuclein in different aggregation states. *J Parkinsons Dis* **1**, 359-371, (2011).

712 63 Comellas, G., Lemkau, L. R., Zhou, D. H., George, J. M. & Rienstra, C. M. Structural
713 intermediates during alpha-synuclein fibrillogenesis on phospholipid vesicles. *J Am*
714 *Chem Soc* **134**, 5090-5099, (2012).

715 64 Grey, M. *et al.* Acceleration of alpha-synuclein aggregation by exosomes. *J Biol Chem*
716 **290**, 2969-2982, (2015).

717 65 Galvagnion, C. *et al.* Lipid vesicles trigger alpha-synuclein aggregation by stimulating
718 primary nucleation. *Nat Chem Biol* **11**, 229-234, (2015).

719 66 Fusco, G. *et al.* (1)H, (1)(3)C and (1)(5)N resonance assignments of human muscle
720 acylphosphatase. *Biomol NMR Assign* **6**, 27-29, (2012).

721 67 Hell, S. W. & Wichmann, J. Breaking the diffraction resolution limit by stimulated
722 emission: stimulated-emission-depletion fluorescence microscopy. *Opt Lett* **19**, 780-
723 782, (1994).

724 68 Klar, T. A. & Hell, S. W. Subdiffraction resolution in far-field fluorescence microscopy.
725 *Opt Lett* **24**, 954-956, (1999).

726 69 Mahou, P., Curry, N., Pinotsi, D., Kaminski Schierle, G. S. & Kaminski, C. F.
727 Stimulated emission depletion microscopy to study amyloid fibril formation. *Proc. SPIE.*
728 **9331**, 9331OU, (2015).

729 70 Nagle, J. F. & Tristram-Nagle, S. Structure of lipid bilayers. *Biochim Biophys Acta*
730 **1469**, 159-195, (2000).

731

732 **Acknowledgments.** This research was supported by Parkinson's UK (H-1103 to G.F. and
733 C.M.D.), Wellcome Trust (104933/Z/14/Z to A.D. and 089703/Z/09/Z to C.F.K.), the UK
734 Medical Research Council (MR/N000676/1 to G.F., M.V., C.M.D., A.D. and MR/K015850/1
735 and MR/K02292X/1 to C.F.K.) and the UK Engineering and Physical Sciences Research
736 Council (EP/H018301/1 to C.F.K.).

737

738 **Author contributions.** G.F., C.M.D. and A.D. designed the research. G.F., G.S.K., G.V.,
739 C.M.D. and A.D. designed the experiments. G.F., T.P., A.D.S., P.M., A.C. and A.D. performed
740 the experiments. G.F., T.P., A.D.S., P.M., C.F.K., G.S.K., M.V. G.V., C.M.D. and A.D.
741 analysed the data. G.F., C.M.D. and A.D., wrote the manuscript. All authors revised the
742 manuscript critically and approved the final version.

743

744 **Competing Interests** The authors declare that they have no competing financial interests.

745

746

747 **Legends**

748

749 **Figure 1 | CEST experiments probing the membrane interactions of αS_{A30P} and αS_{E46K}.** CEST
750 experiments were recorded at a ^{1}H frequency of 700 MHz (see Materials and Methods), using protein
751 concentrations of 300 μM and 0.06% (0.6 mg ml^{-1}) of DOPE:DOPS:DOPC lipids in a ratio of 5:3:2 and
752 assembled into SUVs. ^{1}H-^{15}N HSQC spectra were recorded by using continuous wave saturation (170
753 Hz or 350 Hz) in the ^{15}N channel at offsets ranging between -28 kHz and +28 kHz; an additional
754 spectrum, saturated at -100 kHz, was recorded as a reference. Data recorded using a saturation
755 bandwidth of 350 Hz are shown here (the data measured using a saturation bandwidth of 170 Hz are
756 shown in **Supplementary Fig. 2**). For comparison, the plots in panels ***b*** and ***e*** are drawn using αS_{WT}
757 data from our previous investigation[28]. (**a-c**) CEST surfaces for αS_{A30P} (**a**) αS_{WT}[28] (**b**) and αS_{E46K} (**c**). (**d-**
758 **f**) CEST saturation along the sequences of αS_{A30P} (**d**), αS_{WT}[28] (**e**) and αS_{E46K} (**f**). The green lines refer to
759 the averaged CEST profiles measured using offsets at +/- 1.5 kHz, and the profiles for +/- 3 kHz and +/-
760 5 kHz are shown in red and black, respectively. (**g-i**) Schematic illustration (see Materials and Methods)
761 of the equilibrium between surface attached/detached local conformations in the membrane-bound
762 states αS_{A30P} (**g**) αS_{WT}[28] (**h**) and αS_{E46K} (**i**). The major differences in the data of αS_{A30P}, αS_{WT} and
763 αS_{E46K} are located in the anchor region. Overall, these three variants of αS maintain the same
764 topological properties at the surfaces of synaptic-like SUVs.

765

766 **Figure 2. | MAS ssNMR spectra of αS_{A30P} and αS_{E46K} bound to SUVs**. (**a**) ^{13}C-^{13}C DARR correlation
767 spectra (aliphatic regions) recorded at -19 ^{o}C using a 50 ms mixing time at a MAS rate of 10 kHz. We
768 used a 1:65 protein:lipid ratio in both cases, and spectra of αS_{A30P} and αS_{E46K} are shown in the left and
769 right panels, respectively. Residues are indicated using the single letter convention. The highest signal
770 intensities in the spectra of the samples studied here were obtained by performing the measurements
771 at -19 ^{o}C. Under these conditions the lipid mixtures used here are in the gel phase[70], enabling ^{13}C-^{13}C
772 DARR spectra to be measured with significantly increased signal-to-noise ratios but without affecting
773 the pattern of chemical shifts; the latter are consistent with those measured at 4 ^{o}C [28]. No variations in
774 the number of observed resonances or in the chemical shifts were observed using protein:lipid ratios
775 ranging from 1:30 to 1:200 [28]. (**b**) ^{1}H-^{13}C correlation via INEPT transfer recorded at 4 ^{o}C at a MAS rate
776 of 10 kHz. The experiments were performed at a ^{1}H frequency of 700 MHz using a ^{1}H/^{13}C 3.2 mm E^{Free}
777 probe. Atom names ca, cb, cg, cd and ce are used for C^{α}, C^{β}, C^{γ}, C^{δ} and Cε atoms, respectively.

778

779 **Figure 3 | Vesicle assembly induced by αS.** (**a**) Molecular details of the double-anchor mechanism
780 described in this work. SUVs of 50 nm in diameter were modelled to mimic as closely as possible the
781 experimental conditions in this study (see Materials and Methods). αS was modelled with the N-terminal
782 anchor in an amphipathic α-helical conformation (red) and bound to the lower vesicle. The region 65 to
783 97 (cyan) of αS was modelled in an amphipathic α-helical conformation bound to the upper vesicle. The
784 C-terminal fragment (residues 98 to 140) and the linker region 26 to 59 are shown in pink and grey
785 colours, respectively. With this topology the modelling reveals that a single αS molecule could
786 simultaneously bind two vesicles that are up to 150 Å apart. (**b-c**) Cryo-EM (**b**) and STED (**c**) images
787 acquired on SUVs at a concentration of 0.6 mg/ml. (**d-e**) Cryo-EM (**d**) and STED (**e**) images measured

on SUVs following a 12 h incubation with 200 μM αS_{WT}. (**f-g)** Cryo-EM (f) and STED (**g**) images acquired on SUVs following a 12 h incubation with 200 μM αS_{Sw}.

Figure 4 | Stepwise representation of SUV interactions and fusion promoted by αS. The scheme shows the stepwise mechanism of vesicles assembly as probed from images obtained *in vitro* by cryo-EM, which are also shown. Disordered cytoplasmatic αS (red) binds dynamically to the surface of SUVs (green), as described in this study. SUVs coated with αS assemble with fast kinetics as a consequence of the double-anchor mechanism promoted by the αS molecules decorating their surfaces. The tethered SUVs, which are initially assembled together in dimeric, trimeric, tetrameric and higher order states, eventually fuse to form larger vesicles. With the increasing size of the fused vesicle, we could observe preferential fusion events at the termini of the aggregated vesicles. This observation can be explained by the higher affinity of αS for significantly curved membrane surfaces[19], which increases the concentration of bound αS at the termini of the elongated vesicles thereby promoting a stronger double-anchor mechanism in these loci.

Figure 5 | Clustering of synaptic vesicles promoted by αS. SVs purified from rat brain were incubated for 48h at 37°C. The concentrations during the incubation were 0.5 mg ml^{-1} and 85 μM for the SVs and the αS variants, respectively. (**a-c**) *d*STORM imaging of SVs alone (**a**) and SVs incubated with αS_{WT} (**b**) and with αS_{Sw} (**c**). The images were collected using a previously described protocol[46]. Scale bars indicate 1 μm. In order to generate fluorescent SVs, we used a primary antibody that is specific for synaptotagmin 1 and a secondary antibody that is covalently linked to an ATTO 647N dye. 10,000 fluorescence frames with an exposure time of 10 ms were recorded. The field of view imaged covered 1997 × 1997 camera pixels, corresponding to an area on the sample of ~20 × 20 μm^2. (**d**) To assess the level of clustering of the SVs, we adapted an approach that has previously been successfully employed to analyse protein self-assembly. For each *d*STORM image, clusters of SVs were identified on the basis of the distances between the centers of mass of the SVs. In particular two or more vesicles were associated with a specific cluster if their distances apart are less than 60 nm. The distribution of SVs in clusters of different sizes is reported using orange, green and blue histograms for SVs, SVs in the presence of αS_{WT} and SVs in the presence of αS_{Sw}, respectively. Cryo-EM images (scale bar of 50 nm) show representative clusters of different size.

Tables

Table 1. Primers Used in this Study

Primer Name	Variant	Sequence	Tm (°C)
K80E_F	αS_{Sw}	5'-AGTAGCCCAGGAGACAGTGGAG-3'	65
K80E_R*	αS_{Sw}	5'-GCTGTCACACCCGTCACC-3'	66
A30P_F	αS_{A30P}	5'-GGCAGAAGCACCTGGAAAGACAAAAG-3'	56
A30P_R*	αS_{A30P}	5'-ACACCCTGTTTGGTTTTC-3'	57
E46K_F	αS_{E46K}, αS_{Sw}	5'-CAAAACCAAGAAGGGAGTGGTG-3'	60
E46K_R*	αS_{E46K}, αS_{Sw}	5'-GAGCCTACATAGAGAACAC-3'	57

*reverse primer

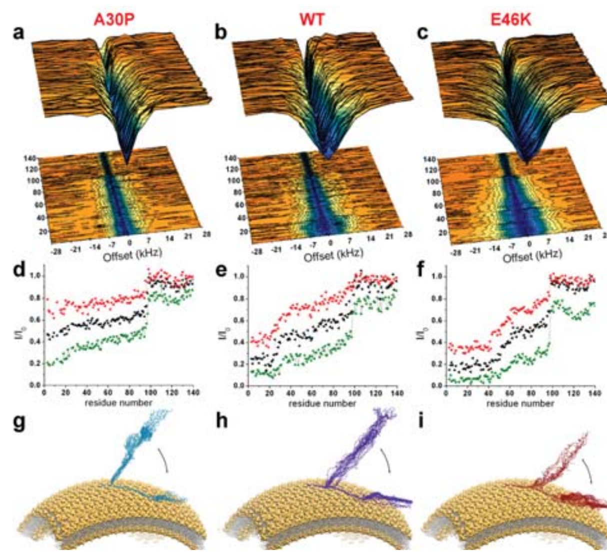
A30P
WT
E46K
a
b
c
Offset (kHz)
d
e
f
I/I_0
residue number
g
h
i

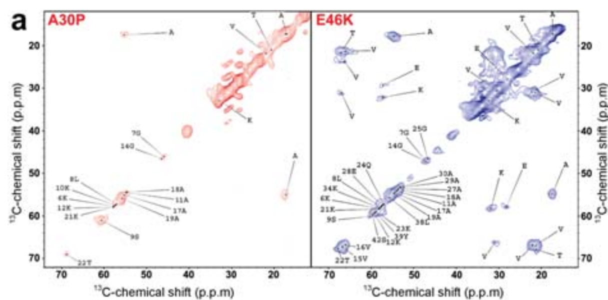
a
A30P
E46K
^{13}C-chemical shift (p.p.m)
^{13}C-chemical shift (p.p.m)

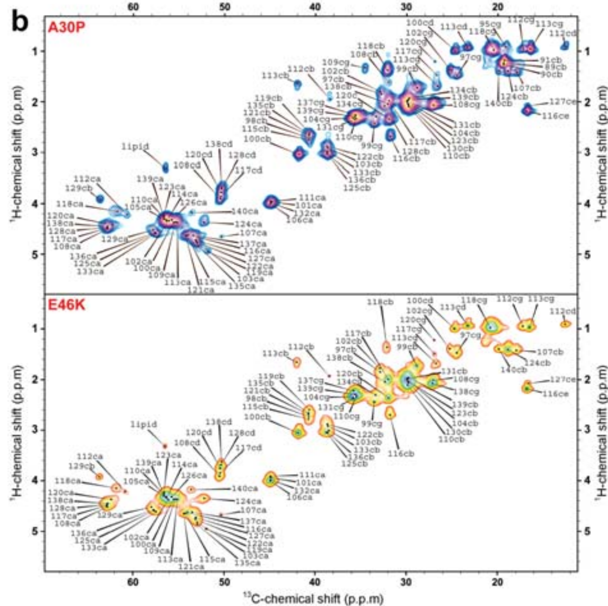
b
A30P
E46K
^{1}H-chemical shift (p.p.m)
^{13}C-chemical shift (p.p.m)

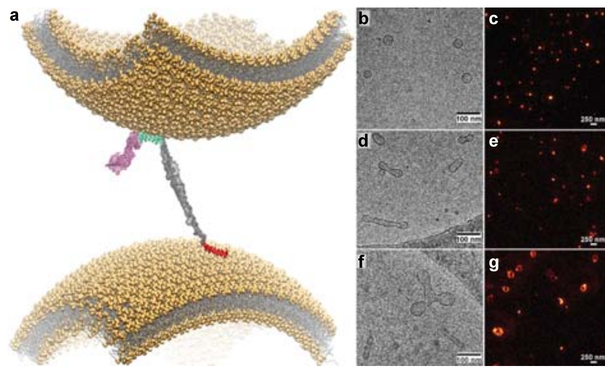
a
b
c
d
e
f
g
100 nm
250 nm
100 nm
250 nm
100 nm
250 nm

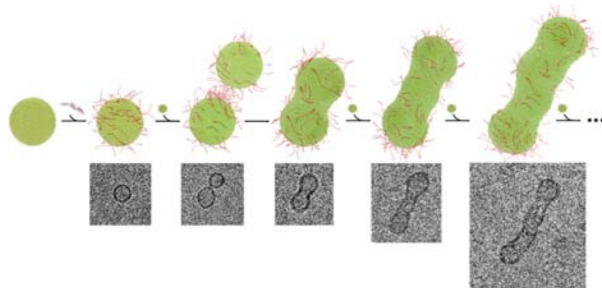

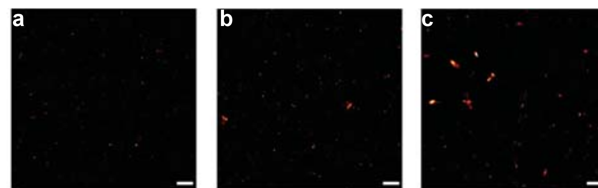
a
b
c

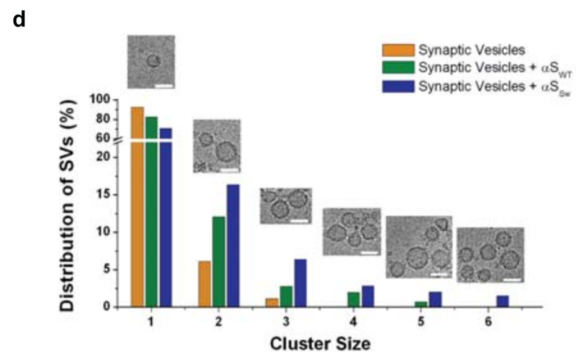
d
Synaptic Vesicles
Synaptic Vesicles + αS_WT
Synaptic Vesicles + αS_Sw
Distribution of SVs (%)
100
80
60
20
15
10
5
0
1
2
3
4
5
6
Cluster Size